International Journal of
INTELLIGENT SYSTEMS AND APPLICATIONS IN ENGINEERING
ISSN:2147-6799 www.ijisae.org Original Research Paper

Design and Development of Nanogenerator for Energy Harvesting Applications

V. Vijayalakshmi[1], Dr. K. S . Geetha[2], Dr. Shanmukha Nagaraj[3]

Submitted: 16/05/2024 **Revised**: 29/06/2024 **Accepted**: 09/07/2024

Abstract: Emerging technology known as a triboelectric nanogenerator (TENG) has the potential to transform mechanical energy into electrical power. It works on the principle of the triboelectric effect, in which electrical charges are created when two different substances come into contact and then break apart. For a simulation-based approach to enhancing the performance of TENG energy harvesting devices, COMSOL Multiphysics software is recommended. The triboelectric effect, which happens when two different substances interact and then separate, is what makes it work. It is hypothesized that a simulation method made possible by the program COMSOL Multiphysics may improve the efficiency of TENG energy harvesting systems. The results of the simulations serve as a guide for the design optimization process, providing important insights into the system's behavior. This research focuses on polymer materials, the primary constituents of nanogenerators. Flexible, lightweight, inexpensive, and easily fabricated polymer materials are ideal for nanogenerator applications. Because of these features, they may be integrated into mobile gadgets, sensors, and flexible electronic systems. We employed widely-available polymer compounds such as polydimethylsiloxane (PDMS), polyvinylidene fluoride (PVDF), trifluoro ethylene (TrFE), and polyvinyl alcohol (PVA). The chosen polymer is subsequently processed into thin films, fibers, or nanowires with enhanced piezoelectric properties. This technique also permits the exploration of fresh methods to improve overall performance. TENG construction and operating parameters may be modified to greatly enhance energy conversion efficiency and power output. The results demonstrate the polymer-based nanogenerator's ability to produce power in the microwatt to milliwatts range, making it well-suited for low-power applications. Incorporating TENG-based techniques, which enhance power-producing capacity, allows for even bigger power outputs. The simulation outcomes provide the foundation for the design optimization procedure and give valuable insights into the system's behavior. Additionally, building a Verilog-A model was motivated by the analytical model's correctness, which allowed the device to be evaluated under various loading circumstances, such as simple resistive and capacitive loads. The technique allows for the investigation of novel approaches to enhancing performance as a whole. Energy may be effectively converted, and new avenues for energy harvesting can be explored by using TENG concepts and matching polymer materials with appropriate electrode materials and mechanical structures.

Keywords: *Triboelectric Nanogenerator (TENG), COMSOL Multiphysics Software, Energy Harvesting and Polymers*

1. Introduction

The idea of energy harvesting has come to light as a potential way to meet the constantly increasing need for power while minimizing our dependency on conventional fossil fuels in the search for sustainable and renewable energy sources. Nanogenerators have caught the attention of researchers and engineers alike among the wide range of energy harvesting technologies because of their exceptional capacity to gather ambient energy from the environment and transform it into useful electricity [1]. These tiny gadgets have opened up fascinating possibilities for redefining how we perceive and use energy in the future, as well as for powering low-energy technological devices. Researchers are looking at Energy harvesting from easily accessible sources, like mechanical vibrations, thermal fluctuations, and ambient electromagnetic fields, has come to be novel solutions to the energy issue as a result of the depletion of traditional energy sources and the urgent need to counteract the negative consequences of climate change [2].

recognized as a promising and sustainable alternative. Nanogenerators, a remarkable device capable of transforming minute amounts of mechanical or thermal energy into electrical power through the clever exploitation of nanoscale phenomena, have taken center stage in this developing field [3].

The fundamentals of piezoelectricity, triboelectricity, and pyroelectricity provide the basis of nanogenerators. These basic ideas have been harnessed and cleverly built at the nanoscale to produce devices that can produce electrical energy from regular mechanical activity like finger tapping, footsteps, or even the lightest wind [4].

[1*]*Research Scholar, ECE Department, RV College of Engineering, Bangalore, Email: Viji14june88@gmail.com*
Assistant Professor, CSE Department Atria Institute of Technology.
[2]*Professor & Vice-Principal, ECE Department RV College of Engineering, Bangalore, Email: geethaks@rvce.edu.in*
[3]*Professor & Dean Academics, Mechanical Department, RV College of Engineering, Bangalore, Email: shanmukhan@rvce.edu.in*
***Corresponding Author:** V. Vijayalakshmi*
**Research Scholar, ECE Department, RV College of Engineering, Bangalore Email: Viji14june88@gmail.com*

Nanogenerators have the potential to run a variety of autonomous, energy-efficient devices without the use of batteries or other external power sources by utilizing the energy that is all around us but frequently goes to waste. One of nanogenerators' most important benefits is their adaptability [5]. They can be easily incorporated into many types of materials, structures, or even clothes, creating a wide range of options for creative uses in numerous industries. Self-powered wearable electronics, for instance, are already a reality. They continuously collect energy from body movements to charge personal electronics, such as cell phones or fitness monitors [6]. Additionally, nanogenerators have shown promise in powering wireless sensors for monitoring the environment, the health of structures, and even implantable medical devices, ushering in a new era of self-sustaining and interconnected smart systems [7].

Additionally, nanogenerators provide a greener option to conventional battery technology by limiting the environmental impact of hazardous battery disposal and lowering electronic waste. Nanogenerators extend the life of electronic equipment while reducing the strain on the resources of our world by offering a permanent and self-renewing energy source. The effectiveness, robustness, and scalability of nanogenerators are being improved as research in nanotechnology and materials science advances [8-9]. To improve energy conversion efficiency and guarantee reliable performance under a variety of environmental circumstances, efforts are being undertaken to optimize the selection of nanomaterials and their integration into the device's architecture. Additionally, improvements in fabrication methods like nanoimprint lithography and additive manufacturing are paving the road for the mass manufacture of nanogenerators, boosting the likelihood of their commercial feasibility [10].

The triboelectric nanogenerator (TENG) converts mechanical energy into electrical power. COMSOL Multiphysics software simulates TENG energy harvesting devices employing polymer materials such as PDMS, PVDF, TrFE, and PVA. Simulations optimize design, power output, and energy conversion efficiency for low-power mobile devices and sensors. TENG-based approaches increase power production, and pairing polymer materials with compatible electrodes and architectures opens new energy harvesting paths.

The remaining components of the study might be classified into the following groups: We will discuss the related works in Section 2. In Section 3 of this paper, the Experimental are addressed. Section 4 presents the MATLAB CAD Software. Section 5 presents the Result. Finally, section 6 is the conclusion of this paper.

2. Related Works

The study [11] created a nanohybrid of PVDF and PZT for use in energy harvesting; a film was produced using a solution casting technique. The high electrical result of the device is a result of the electroactive filler; utilizing 30 wt. % of piezo-filler yields the highest result. The study [12] used common textile components and production techniques to create a TENG device based on textile fabric. These include Teflon, nylon, and fabric production technologies. Improving the overall contact area of the TENG gadget enhanced its electrical efficiency. The triboelectric layer is charged as a result of the contact area. The study [13] presented a paper-based, eco-friendly piezoelectric nanogenerator (PENG) based on a polymer made of zinc oxide (ZnO). According to the findings, the pure ZnO PENG device has an optimal outcome voltage of 2.15 V and a current of 17 nA. The study [14] reported the successful coprecipitation synthesis of magnesiochromitenanocrystalline powder ($MgCr_2O_4$) employing an eggshell membrane as a model for optimized structural and morphological features. Human tapping movements were used to gauge the nanogenerator's potential use as an energy harvester. The study [15] introduced a stretchy, portable, multi-mode triboelectric nanogenerator (msw-TENG) for biomechanical energy harvesting and monitoring of physiological processes. The suggested MSW-TENG has promising applications in future exercise monitoring and rehabilitation therapy since it is a multifunctional biological active sensor that does not require an external power source. The study [16] looked at how the addition of transition metal dichalcogenides (TMDs) improved the piezoelectric polar crystalline phase of PVDF.PVDF–TMD composite films were found to have higher remnant polarisation than PVDF film. The study [17] employed a continuous-wave fiber laser operating at 1064 nm to create tiny designs on a PET substrate. Designed TENG device's efficient output efficiency has been verified by theoretical simulation. Therefore, the suggested TENG is safe and well-suited for use with low-power electronics. The research [18] involved the preparation of composites fibers from 1, 3, 5, 7, and 10% wt% concentrations of polyvinylidene difluoride (PVDF) and cobalt ferrite ($CoFe_2O_4$) nanoparticles (NPs: 16 nm diameter) for use in fabricating flexible PVDF/$CoFe_2O_4$ oriented nanogenerators. There is hope for the future of wearable electronics in the form of newly developed nanogenerators that can generate electrical impulses in response to both mechanical and magnetic stimulations. The study [19] demonstrated a hybrid nanogenerator that combines three distinct approaches to transforming mechanical energy into electrical power. Analyses of the hybrid nanogenerator's charge efficiency revealed that it

greatly increased the voltage level and charge speed of the tested capacitors compared to standalone units. The Study [20] presented a simple delignification procedure that yields a wood sponge that may be used to create a low-cost, biodegradable, biocompatible, and highly compressible piezoelectric nanogenerator. By showcasing our nanogenerator's use as both a wearable movement monitoring system and a large-scale prototype with an improved output capable of powering simple electronic devices, they prove the device's adaptability and use. The study [21] suggested a particular type of origami tessellation (OT) foundation to improve the TENG's electric results efficiency and make it easier to apply it to road pavement for energy collecting. The results of their study provided a revolutionary OT-TENG design that has the potential to significantly improve the results efficiency of TENGs devices in a broader range of shape spaces and environments. The study [22] presented a galloping triboelectric nanogenerator (GTENG) that uses contact electrification between two flexible beams to significantly improve the TENG's efficiency at minimal wind velocities. They show that GTENG's excellent result effectiveness holds even when the wind speed is low. The study [23] developed an innovative and straightforward CNF-based gear-like triboelectric nanogenerator (TENG) by treating cellulose nanofibrils (CNFs) with a surface amino alteration and silver nanoparticle coating. The research demonstrated a high-performance TENG with a gear-like structure and uses it for autonomous sensing. The study [24] presented a soft triboelectric nanogenerator (TENG) that can be printed using a simple all-in-one technique as a potential means of meeting the needs of a wide range of self-powered sources and energy harvesting devices. The study [25] introduced a novel platform of hybrid generators aimed at energy harvesting as a portable practical power source, which might be used for a variety of purposes, including but not limited to navigation and lighting.

3. Experimental

Triboelectric Nanogenerators (TENGs) are a potential technology for energy harvesting that uses triboelectric and electrostatic principles to transform mechanical energy into electrical energy (Figure 1). TENGs are made of two materials, one positively and the other negatively charged, with distinct electron affinities that are separated by an insulating layer. These materials create a potential difference when they come into contact and then separate, which causes an electron flow and the production of electricity. The TENG's effectiveness is due to its capacity to salvage energy from a variety of sources, including human motion, vibrations, wind, and water flow. TENGs are useful for powering small, low-energy devices or sensors in distant or difficult locations where conventional power sources are impractical or unavailable due to their adaptability.TENGs provide many benefits because of their simplicity, scalability, and lightweight. To gather energy from daily activities, they can be included in infrastructure, wearable tech, and clothes. This will lessen the demand for batteries and electrical trash. TENGs continue to increase in efficiency and dependability as nanotechnology research develops, making them a promising and long-term solution to the world's rising energy need.

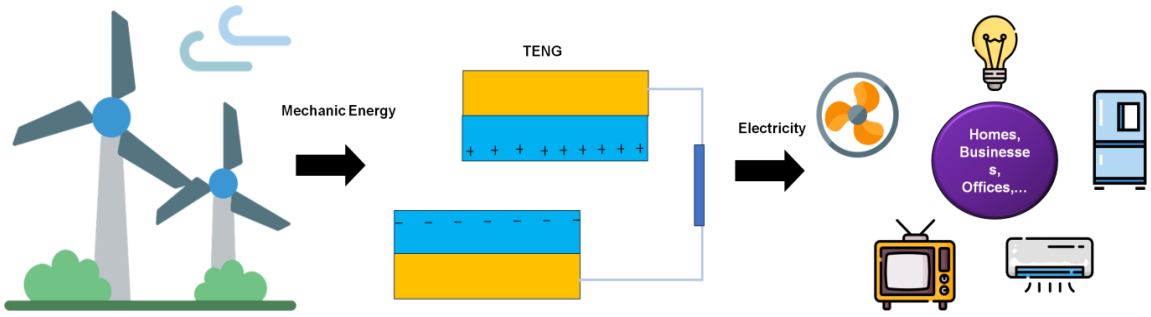

Fig 1: Triboelectric Nanogenerators (TENGs)

We used commercially accessible polymers such as polydimethylsiloxane (PDMS), polyvinylidene fluoride (PVDF), trifluoro ethylene (TrFE), and polyvinyl alcohol (PVA).

3.1 Proposed diagonal model

Due to the similarity between the diagonal mode of the TENG and the fundamental modes of the associated electrodes, the structure of the triboelectric pair can be either a "conductor-dielectric or a dielectric-dielectric." However, the scenario of movement is where the diagonal mode truly stands apart. Instead of being limited to horizontal and vertical motion, it also allows for movement at an angle theta between 0 and 90 degrees. The dielectric-dielectric structure will be discussed and thoroughly explained throughout this research because the same ideas apply to the conductor-dielectric framework with only a few key distinctions. It

has four layers total, including “two dielectrics and two metals." It is between the “two dielectrics” where the charge transfer occurs, making them the tribo-pair.

When two dielectrics come into contact, static charges of “opposite polarity” $(+\sigma, -\sigma)$ and equal density are generated on their surfaces. When the metals are electrically coupled and the “tribo-pair is divided by a mechanical force, a potential difference

(U_{OC}) develops between them, requiring the transfer of charges of magnitude Q. However, this potential difference will decrease when separation distances are reduced. The first source of control over the voltage between the electrodes comes from the static polarizing charges generated by the dielectrics, which establish a possible variation of $(U_{OC}(\theta))$ between the electrodes. Another source of voltage of equivalent magnitude to $\frac{-R}{D(\theta)}$ comes from the capacitor of the structure itself, with Q charges transmitted. The potential difference between the electrodes is calculated using the superposition principle and the following equation (1):

$$U = \frac{-R}{D(\theta)} + U_{OC}(\theta) \tag{1}$$

Therefore, a closed form $(U - R - \theta)$ relation cannot be attained without also acquiring $D(\theta)$, which requires acquiring (θ). The structure has been air-insulated.

3.2 Analytical Model

Figure 2 depicts the equivalent circuit for "the attached electrode diagonal mode with air insulation," which consists of “four capacitors connected in parallel”: C1, among“the top and bottom electrodes”; C2, among“the top electrode and the right wall”; C3, among“the top electrode and the left wall”; and C4, among“the top electrode and the top wall." As a result, adding the charges on the four capacitors yields the total charge in Equation (2).

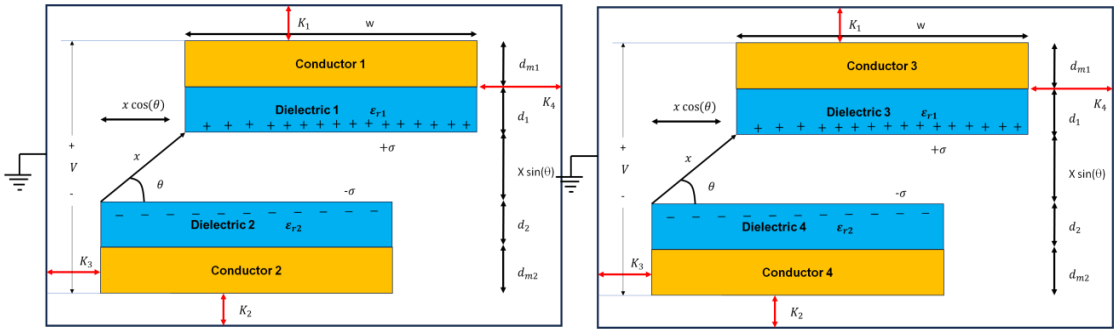

Fig 2: The air-insulated dielectric-dielectric diagonal TENG's 2D model.

$$R_{SC} = R_{SC_1} + R_{SC_2} + R_{SC_3} + R_{SC_4} \tag{2}$$

Equation (1) is the governing equation for TENG,

$$R_{SC} = U_{PD} \times D \tag{3}$$

$$R_{SC} = U_{OC_1} c_1 + U_{OC_2} c_2 + U_{OC_3} c_3 + U_{OC_4} c_4 \tag{4}$$

By analyzing the charge distribution, we may calculate U_{OC} for each capacitor. The dielectric produces opposing charges on the conductor at the nonoverlapped part of the structure. The total charge for every conductor should be zero in an OC state, and this fact ultimately determines the charge at the overlapping region.

If we assume that the overlapping portions of “the top and bottom electrodes” have charge densities B and A, then we need to do the following to meet the OC condition in Equation (5):

$$\sum R_{top} = -\sigma w cos\ (\theta)k + B\big(\omega - wcos(\theta)\big)k = 0 \tag{5}$$

$$\sum R_{bottom} = \sigma w cos\ (\theta)k + A\big(\omega - wcos(\theta)\big)k = 0 \tag{6}$$

To calculate the surface charge density, we plug in the dimensions of the device (width and length), whereas x represents the diagonal distance. As a result, B and A equal in Equation (7),

$$B = \frac{\sigma w cos\ (\theta)}{(\omega - wcos(\theta))}, A = \frac{-\sigma w cos\ (\theta)}{(\omega - wcos(\theta))} \tag{7}$$

Gauss's law is used to calculate the electric field in the z-direction between “the top conductor, first dielectric, air gap, second dielectric, and bottom conductor” of “the first capacitor between the first and second conductors” as in Equation (8),

$$\oint F.DB = \frac{Q_{enclosed}}{\varepsilon_0} \tag{8}$$

Where F is the “electric field," dB is the “smallest unit of the surface area," $Q_{enclosed}$ is the “charge contained within the surface of interest," and ε_0 is the “permittivity

of vacuum." To begin, let's derive F_1, the electric field within the top conductor in Equation (9):

$$-F_1\big(\omega - wcos(\theta)\big)k = \frac{B(\omega - wcos(\theta))k}{\varepsilon_0} \tag{9}$$

$F_1$is equal to in Equation (10)

$$F_1 = \frac{-B}{\varepsilon_0} = \frac{-\sigma wcos\,(\theta)}{\varepsilon_0(\omega - wcos(\theta))} \tag{10}$$

Then, the electric field F_2 within the first dielectric can be calculated as in Equation (11),

$$-F_2\big(\omega - wcos(\theta)\big)k = \frac{B(\omega - wcos(\theta))k}{\varepsilon_0\varepsilon_{q1}} \tag{11}$$

The first dielectric has a permittivity ε_{q1}. Therefore, F_2equals to as in Equation (12),

$$F_2 = \frac{-B}{\varepsilon_0\varepsilon_{q1}} = \frac{\sigma wcos\,(\theta)}{\varepsilon_0\varepsilon_{q1}\,(\omega - wcos(\theta))} \tag{12}$$

Then, we can calculate the electric field F_3 inside the air gap by Equation (13),

$$-F_3\big(\omega - wcos(\theta)\big)k = \frac{B(\omega - wcos(\theta))k}{\varepsilon_0} + \frac{\sigma(\omega - wcos(\theta))k}{\varepsilon_0} \tag{13}$$

Then F_3equals to Equation (14),

$$F_3 = -\frac{B}{\varepsilon_0} - \frac{\sigma}{\varepsilon_0} = -\frac{\sigma wcos\,(\theta)}{\varepsilon_0(\omega - wcos(\theta))} - \frac{\sigma}{\varepsilon_0} \tag{14}$$

The "electric field"F_4 inside the other dielectric is then calculated as in Equation (15),

$$F_4\big(\omega - wcos(\theta)\big)k = \frac{B(\omega - wcos(\theta))k}{\varepsilon_0\varepsilon_{q1}} \tag{15}$$

Where ε_{q2} is the second dielectric's permittivity, Thus, F_4equals to Equation (16),

$$F_4 = \frac{A}{\varepsilon_0\varepsilon_{q2}} = -\frac{\sigma wcos\,(\theta)}{\varepsilon_0\varepsilon_{q1}\,(\omega - wcos(\theta))} \tag{16}$$

Here we derive F_5 as Equation (17), the electric field within the bottom electrode,

$$F_5\big(\omega - wcos(\theta)\big)k = \frac{A(\omega - wcos(\theta))k}{\varepsilon_0} \tag{17}$$

Then F_5equals to Equation (18),

$$F_5 = \frac{A}{\varepsilon_0} = \frac{-\sigma wcos\,(\theta)}{\varepsilon_0(\omega - wcos(\theta))} \tag{18}$$

The line integral Equations (19-20) are used to calculate,

$$U_{OC} = \int_0^{dn_1 + d_1 + w\sin(\theta) + d_2 + dn_2} F.dy \tag{19}$$

$$U_{OC_1} = -\int_0^{dn_1} F_1.dy - \int_0^{dn_1 + d_1} F_2.dy - \int_{dn_1 + d_1}^{dn_1 + d_1 + w\sin(\theta)} F_3.dy - \int_{dn_1 + d_1 w\sin(\theta)}^{dn_1 + d_1 + w\sin(\theta) + d_2} F_4.dy - \int_{dn_1 + d_1 w\sin(\theta) + d_2}^{dn_1 + d_1 + w\sin(\theta) + d_2 + d_{m2}} F_5.dy \tag{20}$$

In which the first metal electrode has a thickness of dm1 and the second metal electrode has a thickness of dm2. And "the first and second dielectric" layers' thicknesses are denoted by d1 and d2 here. Substituting the electric field formulas derived from Equation (7) with the values of A and B, so we get Equation (21),

$$U_{OC_1} = \frac{\sigma wcos\,(\theta)}{\varepsilon_0(\omega - wcos(\theta))}(w\sin(\theta) + d_0 + d_{m1} + d_{m2}) + \frac{\sigma(wcos\,(\theta))}{\varepsilon_0} \tag{21}$$

With $d_0 = {}^{d_1}/_{\varepsilon_{q1}} + {}^{d_2}/_{\varepsilon_{q2}}$definition of d_0 as the dielectric equivalent thickness,

Since the capacitance is primarily determined by the overlapped section of the structure. Capacitance can be calculated as in Equation (22),

$$D_1 = \frac{\varepsilon_0(\omega - wcos(\theta))k}{(w\sin(\theta) + d_0 + d_{m1} + d_{m2})} \tag{22}$$

Gauss's law can be used to determine the electric field in the horizontal(w' -direction) for the other capacitor located between "the top electrode and the right wall" as in Equations (23-24).

$$F_6 d_{m1} k = \frac{-\sigma d_{m1} k}{\varepsilon_0} \rightarrow F_6 = \frac{-\sigma}{\varepsilon_0} \tag{23}$$

$$U_{OC} = -\int_{L_3 + w\,cos\,(\theta) + x + L_4}^{L_3 + w\,cos\,(\theta) + x} F_6 d\,w' = \frac{-\sigma}{\varepsilon_0} L_4 \tag{24}$$

Where L_3 and are "the air insulation distances between the lower and upper electrodes" and the left and right walls, respectively. Using the formula for a parallel plate capacitor, we get the capacitance Equation (25),

$$D_2 = \frac{\varepsilon_0 d_{m1} k}{L_4}$$

(25)

Gauss's law is used to calculate Equations (26-27)"the electric field in the (w'-direction)" for the third capacitor, which is situated between the "top electrode and the left wall."

$$-F_7 d_{m1} k = \frac{B d_{m1} k}{\varepsilon_0} \rightarrow F_7 \frac{B}{\varepsilon_0}$$

(26)

$$U_{OC_3} = -\int_0^{L_3 + w\cos(\theta)} F_7 d\, w' = \frac{\sigma w cos\,(\theta)}{\varepsilon_0(\omega - wcos(\theta))}\,(L_3 + w\cos(\theta)) \quad (27)$$

Capacitance is calculated as follows in Equation (28),

$$D_3 = \frac{\varepsilon_0 d_{m1} k}{L_{3+x\,cos\,(\theta)}} \quad (28)$$

The value of "the fourth capacitor, located between the top electrode and the upper wall" is obtained in Equation (29) by applying Gauss's law under OC conditions to the circuit.

$$F_8 \omega k = \frac{R_{enclosed}}{\varepsilon_0} = 0 \rightarrow F_8 = 0 \quad (29)$$

Capacitance is thus calculated to be in Equation (30), and VOC4 = 0,

$$D_4 = \frac{\varepsilon_0 \omega k}{L_1} \quad (30)$$

The "air insulation distance at the top electrode and the top wall" is denoted by k1. Therefore, R_{SC} determined Equation (31)to be by applying Equation (4),

$$R_{SC} = \sigma k w \cos(\theta) + \frac{(\sigma k w \sin(\theta)(\omega - w\cos(\theta))}{(w\sin(\theta) + d_0 + d_{m1} + d_{m2})} - \sigma d_{m1} k + \frac{\sigma d_{m1} k w cos\,(\theta)}{(\omega - w\cos(\theta))} \quad (31)$$

In addition, the "four parallel capacitors" are comparable to the overall capacitance of the building as in Equations (32-33),

$$D_{Total} = D_1 + D_2 + D_3 + D_4 \quad (32)$$

$$D_{Total} = \frac{\varepsilon_0(\omega - wcos(\theta))k}{(w\sin(\theta) + d_0 + d_{m1} + d_{m2})} + \frac{\varepsilon_0 d_{m1} k}{L_4} + \frac{\varepsilon_0 d_{m1} k}{L_3 + w\,cos\,(\theta)} + \frac{\varepsilon_0 \omega k}{L_1} \quad (33)$$

Finally, the U_{OC} can be calculated as follows: $U_{OC} = R_{SC}/D_{Total}$. The closed-form $(U - R - \theta)$relation can be found by substituting the values indicated in Equation (31) for R_{SC} and Equation (33) for D_{Total} as in Equation (34),

$$\frac{1}{\left(D_{Total} = \frac{\varepsilon_0(\omega - wcos(\theta))k}{(w\sin(\theta) + d_0 + d_{m1} + d_{m2})} + \frac{\varepsilon_0 d_{m1} k}{L_4} + \frac{\varepsilon_0 d_{m1} k}{L_{3+x\cos(\theta)}} + \frac{\varepsilon_0 \omega k}{L_1}\right) \times \left(-R + \sigma k w \cos(\theta) + \frac{\sigma k (w\sin(\theta))(\omega - wcos(\theta))k}{(w\sin(\theta) + d_0 + d_{m1} + d_{m2})} - \sigma d_{m1} k + \frac{\sigma d_{m1} k w\, cos\,(\theta)}{(\omega - wcos(\theta))}\right)} \quad (34)$$

3.3 COMSOL model

In this work, the open circuit voltage and short circuit transferred charge were calculated using the finite element method (FEM) software COMSOL Multiphysics 5.3. The use of electrostatics physics and stationary studies, in which static charges of the two dielectrics' surfaces were treated with$(+\sigma, -\sigma)$, is substituted for COMSOL's lack of physics for the triboelectrification. These four types of dielectrics are polydimethylsiloxane (PDMS), polyvinylidene fluoride (PVDF), trifluoro ethylene (TrFE), and polyvinyl alcohol (PVA), respectively. The simulation's parameters are listed in Table 1; however, they can be altered depending on how the TENG is applied.

In-depth research was done on the structure's short-circuit (SC) and open-circuit (OC) states. Each metal electrode must have a total surface charge density of zero in order to satisfy the OC boundary condition. In the model, this is achieved by choosing the terminal type to be charged and setting$R_0 = 0$. A "zero-electric potential difference" between the two metal electrodes is necessary for the SC boundary condition. By deciding on the voltage value and terminal type, $U_0 = 0$, this was represented in the model. In this simulation, air insulation is also used to encircle the structure, which is also possible in reality.

Table 1: Used as a parameter set throughout the whole COMSOL simulation

Parameter	**Value**
Maximum diagonal angle (θ_{max})	90°
Diagonal distance (x)	100 m
Metal electrodes Thickness (C_n)	1 m

Differences in dielectric strength ($\varepsilon_{q1}, \varepsilon_{q2}$)	$\varepsilon_{q1} = 4$ $\varepsilon_{q2} = 2$
Distances for air insulation (l_1)	2, 3, 4, 1 m
The thickness of the dielectrics (c_1, c_2)	25 m
The density of surface charges (C/cm^2)	100
Device width (w) and length (l)	1 mm
Average angular velocity	1 m/s

3.4 Optimization of Multi-Dimensional Diagonal TENG Performance

Any TENG structure result can be optimized by carefully selecting the resources that are employed. This section seeks to offer information on selecting the appropriate materials, which is a difficult undertaking that greatly depends on the intended purpose of the harvester. It is split into two sections that follow.

3.4.1 The Multi-Dimensional Diagonal TENG's Stored Energy and the Effect of Dielectrics

To get the highest performance, the multi-dimensional diagonal mode attached electrode TENG must have the best possible dielectric combination of the materials that are already on the market. Table 2 lists the investigated materials together with their respective dielectric constants. Two criteria were used to determine which material combinations to study. The first is that it is possible to obtain the ingredients and that they can be produced cheaply and easily in solid form. The following is the isolation of every material pair in the TE series; as a result, when the system is used in practice, a significant quantity of charges is transmitted between them. The TE series is a list of substances arranged in accordance with their propensity to accumulate or discharge charges.

Table 2: Dielectric materials and their constants were researched

Polymer Material	Dielectric Constant
PDMS	2.65
PDVF	8
TrFE	7
PVA	20

Additionally, in order to not be constrained by the discrete values of the dielectric constant (ε_q) of the available dielectric materials, the first part also seeks to identify the values of the two dielectric constants that correspond to the system capable of storing the most energy and performing at its peak. The significant potential for future material discoveries prompted this investigation. The optimal combination of the four dielectrics was determined by varying their dielectric constants from 2 to 6 and then calculating the average stored energy of the structure from all angles.

3.4.2 Performance of Multi-Dimensional Diagonal TENG for Capacitor on Unidirectional Charging

Harvesters, which transform mechanical energy into various forms, cannot be employed directly since even a small change in the harvester's environment may generate an unstable output. As a result, they are frequently coupled to energy storage devices like capacitors. The second part of this article is to enlighten the reader about how capacitors work to stabilize output and what materials may be used to create a dielectric for the TENG's diagonal mode that is also compatible with the energy storage device.

Similar circuit In the case of a capacitive load (D_{Load}), the system's initial conditions are as follows: at time $s = 0$, the top dielectric is in the state of $\theta = 0$ and is just beginning to move, therefore the charges on the "TENG electrodes" at a time $R\ (t = 0)\ 0$ are zero. Additionally, the capacitive load initially has no charges $R_D(t = 0) = 0$. The following equations are obtained by applying "Kirchhoff's rules" and the nodal assessment approach in the circuit:

$$U = \frac{-R}{D_{TENG}} + U_{OC} = \frac{R_D}{D_{Load}} \quad (35)$$

$$\therefore R_D = D_{Load} U \quad (36)$$

$$\because R_D - R = R_D(s = 0) - R(s = 0) = 0 \quad (37)$$

$$\therefore R = R_D = D_{Load}U \quad (38)$$

At the farthest possible division, the capacitor's final voltage and charge are calculated by plugging values into Equation (35) at ($\theta = \theta_{max} = 90$) where $w\ sin(\theta)$is of maximum value.

$$\therefore U_{(\theta=\theta_{max})} = \frac{-D_{Load}U_{(\theta=\theta max)}}{D_{TENG}} + U_{OC,max} \quad (39)$$

$$\therefore U_{(\theta=\theta_{max})} = \frac{D_{TENG}U_{OC,max}}{D_{TENG}+D_{Load}} = \frac{R_{SC,max}}{D_{TENG}+D_{Load}} \quad (40)$$

$$F_D = \frac{1}{2}D_{Load}\left[U_{(\theta=\theta_{max})}\right]^2 = \frac{D_{Load}R_{SC,max}^2}{D_{TENG}+D_{Load}} \quad (41)$$

$$\therefore F_D = \left(D_{Load}\left[\sigma kwcos(\theta) + \frac{\sigma kw\ sin(\theta)(x-w\cos(\theta))}{(w\ sin(\theta)+d_0+d_{n1}+d_{n2})} - \sigma d_{n1} + \frac{\sigma d_{n1}kw\ cos(\theta)}{(x-w\cos(\theta))}\right]^2\right) / \left(2\left[\frac{\varepsilon_0(x-w\cos(\theta))k}{(w\sin(\theta)+d_0+d_{n1}+d_{n2})} + \frac{\varepsilon_0 d_{n1}k}{l_4} + \frac{\varepsilon_0 d_{n1}k}{(L_3+w\cos(\theta))} + \frac{\varepsilon_0 xk}{l_1} + D_{Load}\right]^2\right) \quad (42)$$

The stored energy F_D is transformed into the following form when the separation is at its greatest ($\theta = \theta_{max} = 90$):

$$F_D = \left(D_{Load}\left[\frac{\sigma lwx}{(w+d_0+d_{n1}+d_{n2})} - \sigma d_{n1}k\right]^2\right) / \left(2\left[\frac{\varepsilon_0 xk}{(w+d_0+d_{n1}+d_{n2})} + \frac{\varepsilon_0 d_{n1}k}{l_4} + \frac{\varepsilon_0 d_{n1}k}{l_3} + \frac{\varepsilon_0 xk}{l_1} + D_{Load}\right]^2\right) \quad (43)$$

The same tribo-pairs as in the previous portion are utilized in Equation (43), and the optimal combination is calculated.

3.5 Model for Verilog-A

By using a lumped parameter equivalent circuit model as an ideal arbitrarily time-varying voltage source, $U_{OC}\ (s)$, serially linked to a capacitor $D\left(\theta(s)\right)$, the $U-R-\theta$ model in (34) and the relationships in (31, 32) enable TENG modeling. This idea is demonstrated in Figure 3. The upper component of the diagonal mode, which consists of the upper electrode linked to the upper dielectric, rotates in a manner that can be described by the equation $\theta = \omega s$, whereω is the "angular velocity" and s is the time. The $U-R-\theta$ relationship can be stated as follows when considering the straightforward scenario of a purely resistive network connected to the "TENG system" via its two electrodes:

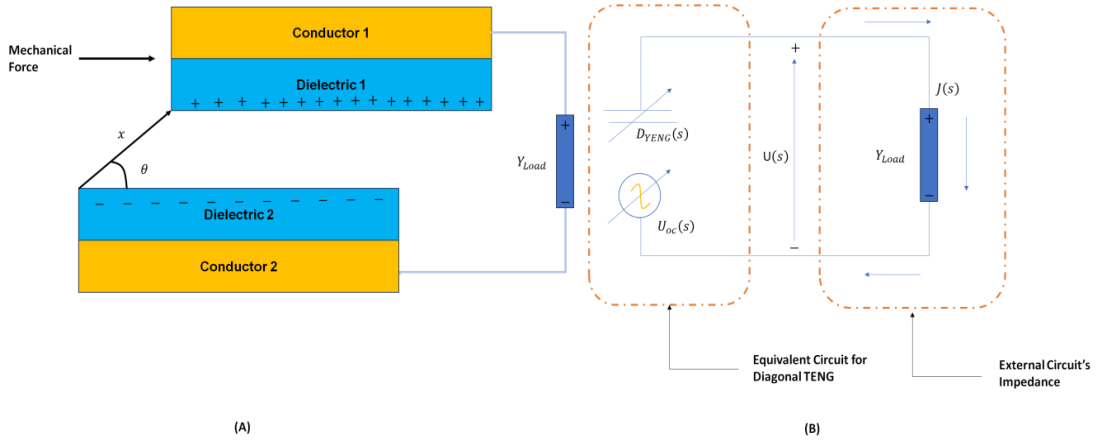

Fig 3: (A) Externally-coupled TENG structure with a diagonal-mode electrode, and (B) a model of the system's equivalent circuit.

$$U = Q\frac{d}{ds}R\left(\theta(s)\right) = -\frac{1}{D(\theta(s))} \times R\left(\theta(s)\right) + U_{OC}\left(\theta(s)\right) \quad (44)$$

$Q$is the "equivalent resistance" visible at the TENG terminals, where. By calculating $J\ (s) = c|\ R\ |/ds\ and\ U\ (s) = Q\ (c|\ R\ |/ds)$, respectively, Waveforms of current and voltage at the TENG-load interface can be calculated. It takes the specific analytical form of $\theta(s)$ to solve the integrals in (44) because they are rather difficult. Additionally, if active elements or other complex loads are linked, the simple equation must be replaced with a more complicated one, the analytical solution of which is difficult and time-consuming to solve using any of the FEM modeling tools. This is because active elements are more complex loads. Therefore, a Verilog-A model of the diagonal mode attached electrode TENG was designed to facilitate the ease with which the TENG structure may be integrated with a wide range of complicated loads for a wide range of applications using various circuit modeling tools.

4. MATLAB CAD Software

The Multi-Dimensional diagonal mode connected electrode TENG requires time-consuming FEM simulation using COMSOL, especially as the harvester's dimensions grow. Based on the confirmed comprehensive analytical model given in this paper—which reveals an average inaccuracy of 5%, 4.7%, and 0.89% for the OC voltage, SC charge, and capacitance, respectively—a new CAD tool is created to offer a quicker alternative. In comparison to COMSOL, this program offers a GUI that makes it easier for users to design TENG harvesters in the future while still being highly efficient. It was created using MATLAB, and Figure 4's flow chart illustrates how it functions.

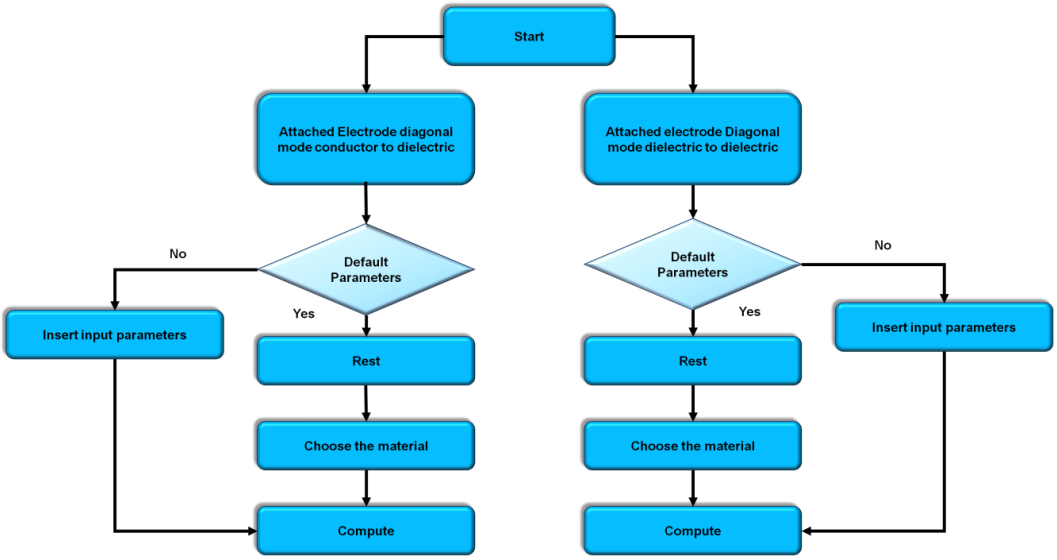

Figure 4: Flow Chart of the CAD Tool

Its primary purpose is to compute the R_{SC} and D of a combined for any user-specified range of parameters and dimensions. Other options include resetting the parameters and dimensions to their default defaults and plotting the results, which enables charting of U_{OC}, R_{SC}, or D vs theta to comprehend how the angle affects the operation of the harvester. Additionally, it generates a set of error messages, such as a range error if the step is inconsistent with the start and finish points, which makes it simpler and more convenient to use the tool appropriately.

5. Result

5.1 Assessment of the Analytical Model

The analytical model is validated by carefully examining the outcomes of the produced analytical model and contrasting them with COMSOL results. The FEM results are in great agreement with the analytical model, with average errors for U_{OC}, R_{SC}, and D of 5.3%, 4.7%, and 0.89%, respectively, as a result of FEM restrictions. Figures 7(a) through (c) show the analytical and simulation results for U_{OC}, R_{SC}, and capacitance, respectively. A second-order filter response characteristic may be seen for both the open circuit voltage and the short circuit charge. The measurements show that the highest OC voltage is 5, the highest SC charges are 45 pC, and the capacitance is practically constant at 9.2 pF.

5.2 Performance Optimization of Multi-Dimensional Diagonal TENG Using Dielectric Materials

The tribopairs employed throughout this study's investigation of the impact of dielectrics on the performance of diagonal TENG are listed in Table 3, along with the total energy they can hold in their systems. Since the maximum angle depends only on the geometry, the maximum stored energy for the geometry employed with the dimensions indicated in Table I is at an angle of 80 degrees for all materials. In comparison to other tribo- pairings investigated in the literature, this one finds that PDFA and TrFE have the best harvester performance, with a maximum energy of 0.40229 nJ.

Table 3: The system's maximum energy storage at various tribo-pairs

Polymer Material	Dielectric Constant
PDMS +PVDF	0.38722
PDMS + TrFE	0.37371
PDMS + PVA	0.35762
PVDF + TrFE	0.40229

PVDF + PVA	0.36987
TrFE + PVA	0.37487

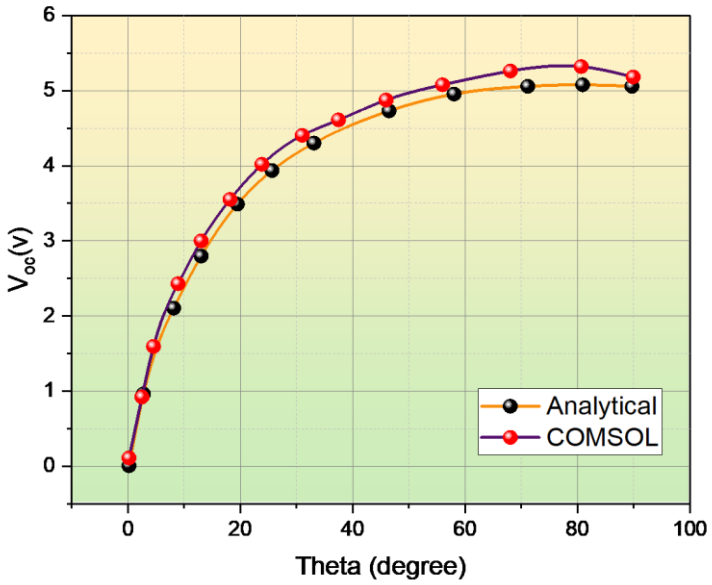

Fig 5: COMSOL simulation results (OC Voltage ($V_{OC}(\theta)$))

As a result, at ⬚and ε_{q2}, the system displays the highest stored energy of 0.3986nJ. This cannot be used in the harvester because it is incompatible with the triboelectrification phenomena, which necessitates the use of two distinct materials. As a result, it is demonstrated that the system with two different dielectric constants has the highest stored energy of 0.3866 nJ with ε_{q1} = 6 and ε_{q2} = 4 9.

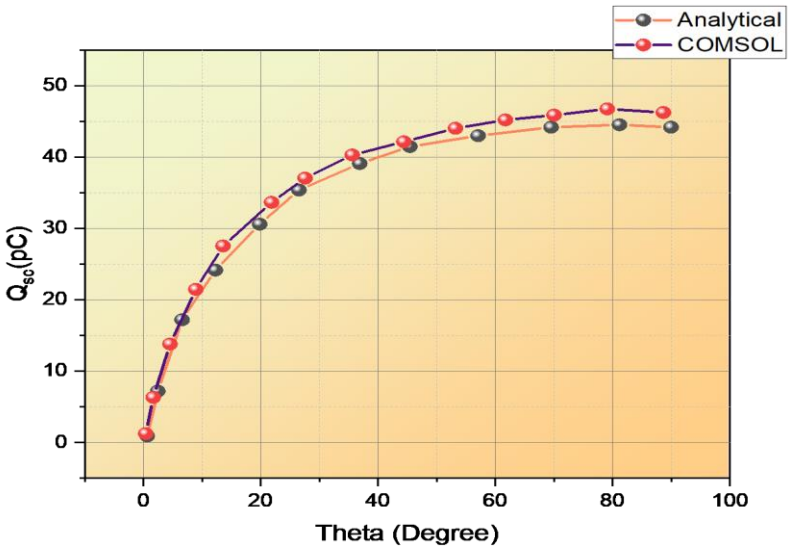

Fig 6: COMSOL simulation results (SC Voltage ($Q_{SC}(\theta)$))

Regarding the efficiency of the diagonal mode TENG in charging a capacitor, the output profile of the capacitor stored energy is shown in Figure 8 for different dielectric materials with different load capacitances ranging from 1 fF to 1 µF. In comparison to the other examined pairings, the Nylon and Kapton pair performs the best, with maximum energy stored of 97.73 pJ at a load capacitance of 8.99 pF. The results demonstrate that the capacitor's stored energy approaches zero at both large and low load capacitances. This outcome is justified because, in the case of a tiny load capacitance (D_K), the impedance is very high and is comparable to that of an open circuit, while the amount of stored energy is relatively low (approaches zero). On the other hand, if D_K is big, it will have a low impedance, which is equivalent to an SC, but it will also have a restricted amount of stored energy because of the low voltage that is supplied to it. Additionally, as shown in Figure 8, the capacitor can store the most energy when $D_K = D_{TENG}$.

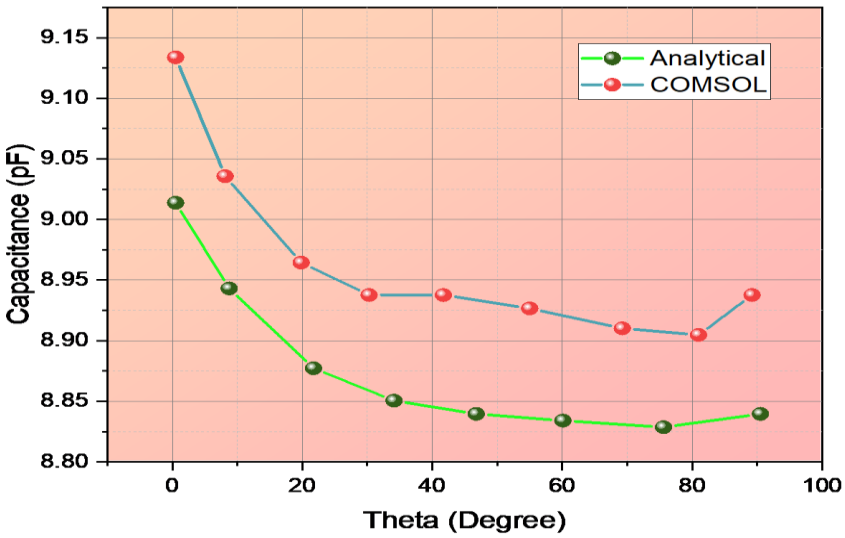

Fig 7: COMSOL simulation results capacitance in its entirety

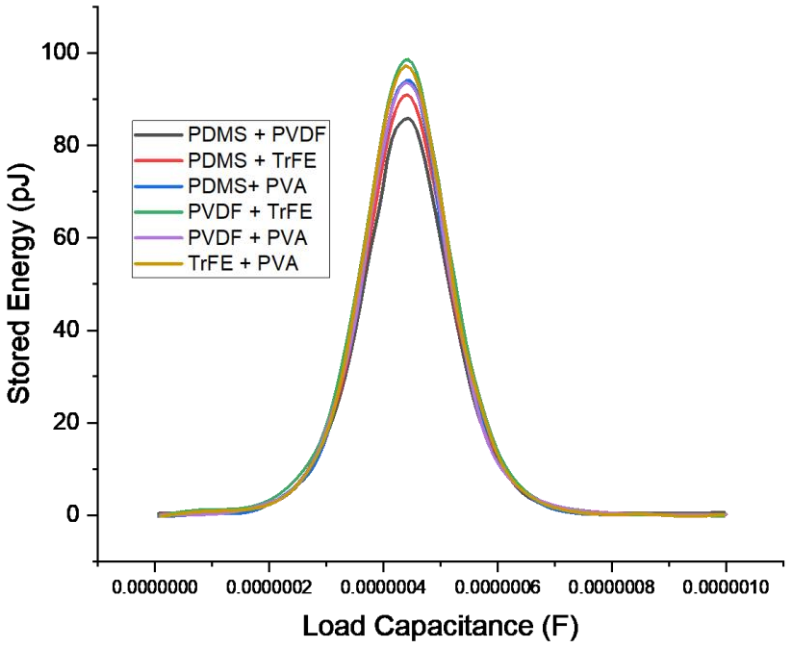

Fig 8: Profile of the Energy Stored in the Capacitor

5.3 Results of Verilog-A Simulation

To explore the features of the harvester under various loading situations, a Verilog-A model was built with the correctness of the derived analytical model as a driving force. Table I lists the parameters that were utilized to run the simulations. U_{OC} has a peak value of 5 V at a value of 90. The voltage response against changes as the resistance value drops, with the voltage peak value fading until it reaches zero at $Q = 0$, SC State. The greatest current measured at $Q = 0$, SC condition, and for $\theta = 0$ is 193 pA. At Q = 100 G, the OC waveform transitions from an underdamped system to an overdamped system as the resistance value rises, and it eventually reaches zero in the OC circumstances. Figure 9 plots the resulting power in pW against resistor values; at Q = 110 G, a 50 pW peak power is seen.

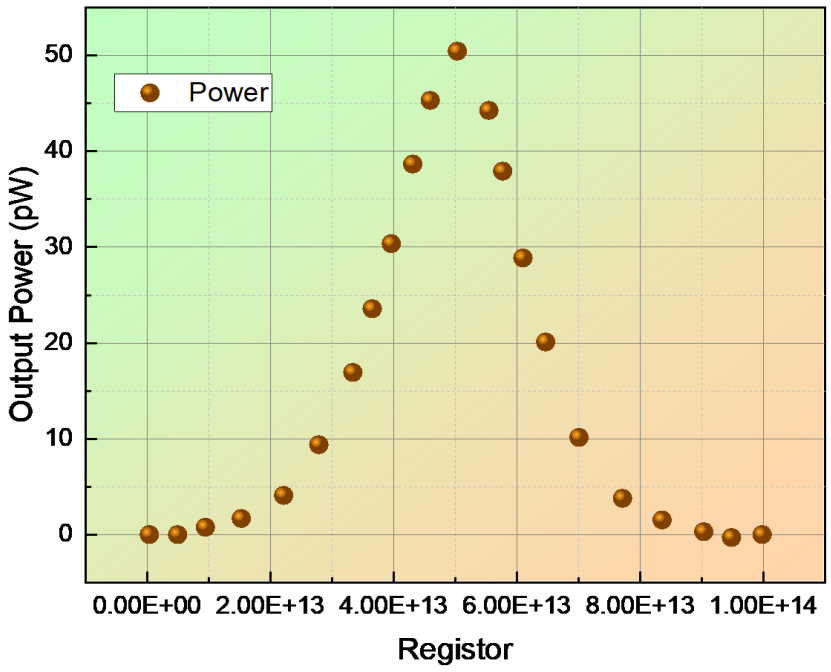

Fig 9: The load resistor's average provided power.

The highest impedance since $Z_c = 1/sC, C = 100\,fF$, is discovered to have a maximum voltage value of 4.5 V. The current number drops off exponentially as one moves from 0 to 90 and eventually hits 0. Peak stored energy of 16 pJ is seen at $C = 9\,pF$ in Figure 10; it graphs the amount of energy stored in the capacitor as a function of its size in pJ. This is anticipated from Figure 7, where it is shown that the device inherited a capacitance of $9\,pF$ and that, in accordance with the maximum power transfer principle, the matched load must be close to the equal value. This is further supported by (41).

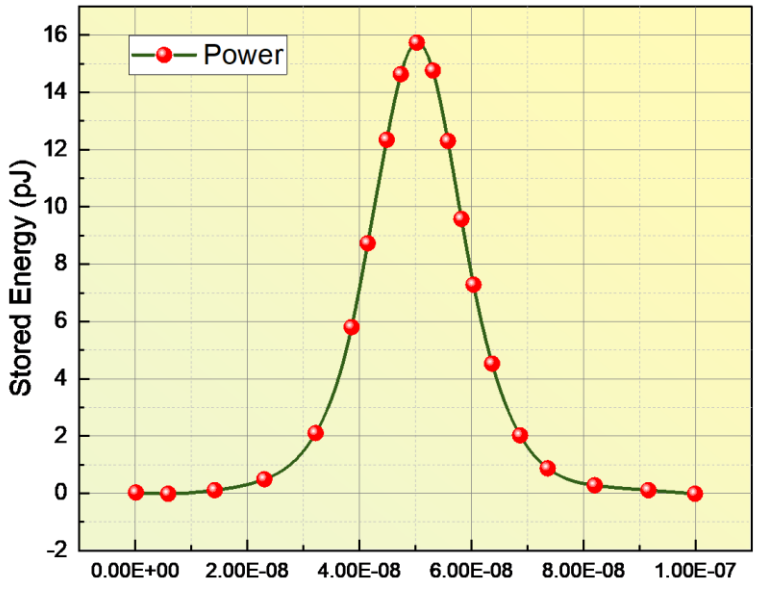

Fig 10: Power delivered to the load capacitor on average.

6. Conclusion

In this investigation, many polymer compounds, including polydimethylsiloxane (PDMS), polyvinylidene fluoride (PVDF), trifluoro ethylene (TrFE), and polyvinyl alcohol (PVA), were used. To improve their piezoelectric qualities and energy conversion effectiveness, these polymers were transformed into thin films, fibers, or nanowires. The results of the simulation produced important details about how the TENG-based systems performed and provided a manual for design optimization. The efficiency of energy conversion and power generation of TENGs may be significantly enhanced by altering their design and operational

characteristics. This enables power production in the microwatt to milliwatt range, making TENGs appropriate for low-power applications. The research found that, compared to the other pairs utilized in the literature, the tribopair of PDVF and TrFE displays the best performance of the harvester, with a maximum energy of 0.40229 nJ. Novel possibilities for energy harvesting are presented by the combination of TENG-based approaches and the matching of polymer materials with relevant electrode materials and mechanical designs. As a result of the accuracy of the analytical model, the device could be tested with both simple resistive and capacitive loads, which in turn inspired the development of a Verilog-A model. These innovations in technology have the capacity to produce significantly greater power outputs, enabling their incorporation into various mobile devices, sensors, and adaptable electronic systems. Exciting new possibilities for efficient energy conversion and the investigation of innovative methods for gathering energy have been made possible by the combination of TENG ideas with simulation-based optimization employing polymer materials.

Future work for this may include additional evaluation and fine-tuning of the simulation-based strategy utilizing COMSOL multiphysics to enhance the functionality and design of TENG harvesting devices. Furthermore, investigating and evaluating innovative polymer and electrode materials may result in even larger enhancements to power output and energy conversion efficiency for a variety of low-power applications.

References

[1] Li, X., Jiang, C., Zhao, F., Lan, L., Yao, Y., Yu, Y., Ping, J. and Ying, Y., 2019. Fully stretchable triboelectric nanogenerator for energy harvesting and self-powered sensing. *Nano Energy*, *61*, pp.78-85.

[2] Hu, S., Chang, S., Xiao, G., Lu, J., Gao, J., Zhang, Y. and Tao, Y., 2022. A Stretchable Multimode Triboelectric Nanogenerator for Energy Harvesting and Self-Powered Sensing. *Advanced Materials Technologies*, *7*(3), p.2100870.

[3] Sun, L., Chen, S., Guo, Y., Song, J., Zhang, L., Xiao, L., Guan, Q. and You, Z., 2019. Ionogel-based, highly stretchable, transparent, durable triboelectric nanogenerators for energy harvesting and motion sensing over a wide temperature range. *Nano Energy*, *63*, p.103847.

[4] Pandey, R., Khandelwal, G., Palani, I.A., Singh, V. and Kim, S.J., 2019. A La-doped ZnO ultra-flexible flutter-piezoelectric nanogenerator for energy harvesting and sensing applications: A novel renewable source of energy. *Nanoscale*, *11*(29), pp.14032-14041.

[5] Ghafari, E., Nantung, T. and Lu, N., 2019. An efficient polyvinylidene fluoride (PVDF) nanogenerator for energy harvesting in the low-frequency range. *ES Materials & Manufacturing*, *5*(2), pp.72-77.

[6] Zhang, Z., Xu, Y., Wang, D., Yang, H., Guo, J. and Turng, L.S., 2019. Enhanced performance of an expanded polytetrafluoroethylene-based triboelectric nanogenerator for energy harvesting. *Nano Energy*, *60*, pp.903-911.

[7] Dong, L., Wang, M., Wu, J., Zhu, C., Shi, J. and Morikawa, H., 2022. Stretchable, adhesive, self-healable, and conductive hydrogel-based deformable triboelectric nanogenerator for energy harvesting and human motion sensing. *ACS Applied Materials & Interfaces*, *14*(7), pp.9126-9137.

[8] Parida, K., Kumar, V., Jiangxin, W., Bhavanasi, V., Bendi, R. and Lee, P.S., 2017. Highly transparent, stretchable, and self-healing ionic-skin triboelectric nanogenerators for energy harvesting and touch applications. *Advanced Materials*, *29*(37), p.1702181.

[9] P. Periyathambi, N. Javed, M. K. Syed Meeral, S. Kiruba, R. Thiagarajan and R. Krishnamoorthy, "Exploring the Experimental Possibilities of LiFi: A Novel IoT based Wireless Data Transmission through Visible Light Communication," *2024 10th International Conference on Communication and Signal Processing (ICCSP)*, Melmaruvathur, India, 2024, pp. 153-158, doi: 10.1109/ICCSP60870.2024.10543880.

[10] A. K. Cherian, S. Devipriya, B. P. Saoji, B. Mallikeswari, R. Thiagarajan and R. Krishnamoorthy, "A Robust Design of Real-Time Resilient Smile Recognition System using Hybrid Deep Learning Principles," *2024 10th International Conference on Communication and Signal Processing (ICCSP)*, Melmaruvathur, India, 2024, pp. 592-596, doi: 10.1109/ICCSP60870.2024.10543446.

[11] V. S. Prakash, R. Vanitha, S. V. Nikam, V. Athappan, R. Krishnamoorthy and S. Arun, "Revolutionizing Agriculture: Artificial Intelligence Assisted Plant Leaf Disease Detection using Deep Learning Principles," *2024 10th International Conference on Communication and Signal Processing (ICCSP)*, Melmaruvathur, India, 2024, pp. 586-591, doi: 10.1109/ICCSP60870.2024.10543984.

[12] V. Balaji Vijayan, T. Dhanalakshmi, P. Parthasarathi, S. Nivedha, R. Krishnamoorthy and R. Thiagarajan, "Experimental Evaluation of Smart Forest Fire Detection Methodology using Internet of Things and Logical Sensors," *2024 10th International Conference on Communication and*

Signal Processing (ICCSP), Melmaruvathur, India, 2024, pp. 603-608, doi: 10.1109/ICCSP60870.2024.10543364.

[13] Suganthy, M., Krishnamoorthy, R., Nagarajaiah, K., & Daya Sagar, K. V. (2024). Lung Cancer Classification based on Auxiliary Classifier (WGAN) Optimised with HOA from CT Images. IETE *Journal of Research*, 1–9. https://doi.org/10.1080/03772063.2024.2352150

[14] Sathiyaseelan, R., Ranganathan, K., Ramamoorthy, R., & Pedda Chennaiah, M. (2024). Haemorrhage diagnosis in colour fundus images using a fast-convolutional neural network based on a modified U-Net. Network: Computation in Neural Systems, 1–22. ttps://doi.org/10.1080/0954898X.2024.2310687.

[15] Ponnan, S., Schmidt, T.W., Li, T., Gunasekaran, H.B., Ke, X., Huang, Y., Mubarak, S., AnandPrabu, A., Weng, Z. and Wu, L., 2021. Electrospunpolyvinylidene fluoride–magnesiochromite nanofiber-based piezoelectric nanogenerator for energy harvesting applications. *ACS Applied Polymer Materials*, *3*(10), pp.4879-4888.

[16] Wu, Y., Li, Y., Zou, Y., Rao, W., Gai, Y., Xue, J., Wu, L., Qu, X., Liu, Y., Xu, G. and Xu, L., 2022. A multi-mode triboelectric nanogenerator for energy harvesting and biomedical monitoring. *Nano Energy*, *92*, p.106715.

[17] Singh, V. and Singh, B., 2020. Fabrication of PVDF-transition metal dichalcogenides-based flexible piezoelectric Nanogenerator for energy harvesting applications. *Materials Today: Proceedings*, *28*, pp.282-285.

[18] Muthu, M., Pandey, R., Wang, X., Chandrasekhar, A., Palani, I.A. and Singh, V., 2020. Enhancement of triboelectric nanogenerator output performance by laser 3D-Surface pattern method for energy harvesting application. *Nano Energy*, *78*, p.105205.

[19] Koç, M., Dönmez, Ç.E.D., Paralı, L., Sarı, A. and Aktürk, S., 2022. Piezoelectric and magnetoelectric evaluations on PVDF/CoFe2O4 based flexible nanogenerators for energy harvesting applications. *Journal of Materials Science: Materials in Electronics*, *33*(10), pp.8048-8064.

[20] Bjelica, J.M., Djuric, N.M. and Djuric, S.M., 2022. Performance analysis and application of a hybrid electromagnetic-triboelectric nanogenerator for energy harvesting. *Energy Reports*, *8*, pp.9184-9200.

[21] Sun, J., Guo, H., Ribera, J., Wu, C., Tu, K., Binelli, M., Panzarasa, G., Schwarze, F.W., Wang, Z.L. and Burgert, I., 2020. Sustainable and biodegradable wood sponge piezoelectric nanogenerator for sensing and energy harvesting applications. *ACS nano*, *14*(11), pp.14665-14674.

[22] Zhang, H., Yang, C., Yu, Y., Zhou, Y., Quan, L., Dong, S. and Luo, J., 2020. Origami-tessellation-based triboelectric nanogenerator for energy harvesting with application in road pavement. *Nano Energy*, *78*, p.105177.

[23] Zhang, L., Meng, B., Xia, Y., Deng, Z., Dai, H., Hagedorn, P., Peng, Z. and Wang, L., 2020. Galloping triboelectric nanogenerator for energy harvesting under low wind speed. *Nano Energy*, *70*, p.104477.

[24] Zhang, C., Lin, X., Zhang, N., Lu, Y., Wu, Z., Liu, G. and Nie, S., 2019. Chemically functionalized cellulose nanofibrils-based gear-like triboelectric nanogenerator for energy harvesting and sensing. *Nano Energy*, *66*, p.104126.

[25] Li, H., Fang, X., Li, R., Liu, B., Tang, H., Ding, X., Xie, Y., Zhou, R., Zhou, G. and Tang, Y., 2020. All-printed soft triboelectric nanogenerator for energy harvesting and tactile sensing. *Nano Energy*, *78*, p.105288.

[26] Yang, H., Deng, M., Tang, Q., He, W., Hu, C., Xi, Y., Liu, R. and Wang, Z.L., 2019. A nonencapsulated pendulum-like paper–based hybrid nanogenerator for energy harvesting. *Advanced Energy Materials*, *9*(33), p.1901149